Mixed-Valence Ruthenium Complexes Rotating Through a Conformational Robin-Day Continuum

Matthias Parthey,[§] Josef B. G. Gluyas,[†] Mark A. Fox,[†] Paul J. Low,[†,||]* and Martin Kaupp[§]*

[§]Technische Universität Berlin, Institut für Chemie, Theoretische Chemie / Quantenchemie, Sekr. C7, Strasse des 17. Juni 135, 10623 Berlin, Germany

[†]Department of Chemistry, Durham University, South Road, Durham DH1 3LE, United Kingdom

[||]School of Chemistry and Biochemistry, University of Western Australia, Crawley, Perth, 6009, Australia.

Abstract

The conformational energy landscape and the associated electronic structure and spectroscopic properties (UV-vis-NIR and IR) of three formally d^5/d^6 mixed-valence diruthenium complex cations, $[\{Ru(dppe)Cp^*\}_2(\mu\text{-}C\equiv CC_6H_4C\equiv C)]^+$, $[\mathbf{1}]^+$, $[\{trans\text{-}RuCl(dppe)_2\}_2(\mu\text{-}C\equiv CC_6H_4C\equiv C)]^+$, $[\mathbf{2}]^+$, and the Creutz-Taube ion, $[\{Ru(NH_3)_5\}_2(\mu\text{-}pz)]^{5+}$, $[\mathbf{3}]^{5+}$, have been studied using a non-standard hybrid density functional BLYP35 with 35% exact exchange and continuum solvent models. For the closely related monocations $[\mathbf{1}]^+$ and $[\mathbf{2}]^+$, the calculations indicated that the lowest-energy conformers exhibit delocalized electronic structures (or class III mixed-valence character). However these minima alone explained neither the presence of shoulder(s) in the NIR absorption envelope nor the presence of features in the observed vibrational spectra characteristic of both delocalized and valence-trapped electronic structures. A series of computational models have been used to demonstrate that the mutual conformation of the metal fragments, and even more importantly the orientation of the bridging ligand relative to those metal centers, influences the electronic coupling sufficiently to afford valence-trapped conformations, which are of sufficiently low energy to be thermally populated. Areas in the conformational phase space with variable degree of symmetry-breaking of structures and spin-density distributions are shown to be responsible for the characteristic spectroscopic features of these two complexes. The Creutz-Taube ion $[\mathbf{3}]^{5+}$ also exhibits low-lying valence-

trapped conformational areas, but the electronic transitions that characterize these conformations with valence-localized electronic structures have low intensities and do not influence the observed spectroscopic characteristics to any notable extent.

Keywords. Conformational phase space, Creutz-Taube ion, mixed-valence transition-metal complexes, Robin-Day scheme, time-dependent density functional theory, valence trapping.

Introduction

Mixed-valence (MV) multinuclear transition-metal complexes are of central importance in the understanding of electron-transfer (ET) processes in nature (e.g. in metalloenzymes), in catalysis, and in the design of functional materials. They have thus attracted the unabated attention of experimentalists and theoreticians[1-5] since the early ground-breaking work on the Creutz-Taube ion and related systems in the 1960s.[6,7] More recently, possible applications in molecular electronics, e. g. as models for molecular wires, have added to the momentum of the field,[8] and organic MV systems also have received increased attention.[1,9-11] A central question in all of these fields is that of the localization of charge on a given redox center (end-cap or bridging ligand) versus delocalization over the molecular framework. In the important model case of two redox centers linked by a bridging ligand, the description of electronic structure is usually made within the Robin-Day scheme,[12] which is based on the extent of electronic coupling of two diabatic localized potential energy curves to give adiabatic ground and excited states of the system (Figure 1). The three primary Robin-Day classes are simply denoted class I, II and III. Class I corresponds to the situation in which there is no coupling between the diabatic potential energy curves. Class II corresponds to partial localization of charge and spin due to the electronic coupling, $2H_{ab}$, being smaller than the (internal plus external) Marcus reorganization energy, λ. This leads to a double-well adiabatic ground-state potential curve with an activation barrier for thermal ET. In contrast, in class III charge and spin are delocalized over both redox centers, and the ground-state barrier has vanished as $2 H_{ab} \geq \lambda$.
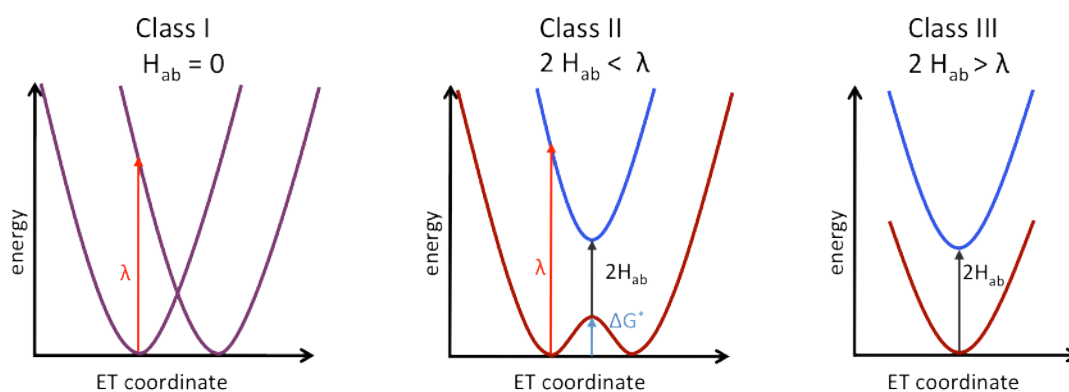
Figure 1. Potential energy surfaces for the three primary Robin-Day classes: Class I (left), class II (middle) and class III (right).

As the optoelectronic properties of a MV system are crucially dependent on the localization/delocalization of charge, the distinctions between class II and III behavior, and especially at the interface between them, has been investigated in detail, through application of an increasingly wide and sophisticated range of spectroscopic and computational techniques and theoretical treatments. The shape and position of the inter-valence charge-transfer band (IVCT; often also designated as MMCT due to the involvement of two metal centers in the classical class II M-bridge-M$^+$ complexes) in optical or near-infrared (NIR) spectra are typically examined in great detail, but given the importance a degree of delocalization of charge over the bridging unit between the two redox centers plays in many systems, metal-bridge CT (metal-ligand CT, MLCT) transitions are also of interest. Other important spectroscopic techniques for the investigation of the electronic character of MV complexes, which involve somewhat different energy and time scales, include vibrational spectroscopies (IR, Raman), Stark spectroscopy, Mössbauer spectroscopy, and electron spin resonance (ESR) spectroscopy. At the borderline between class II and III, small activation barriers and fast ET processes may give rise to contradictory findings with different spectroscopic techniques, due to the different time scales of the spectroscopic methods which can be comparable to the rates of electron-transfer, inner-sphere reorganization processes and solvent dynamics. This convolution of internal reorganization and solvent dynamics has led Meyer and coworkers to introduce an intermediate class II/III which accounts for those systems in which intramolecular electron-transfer rates are faster than outer-sphere solvent rearrangement.[3] Finally, a class IV was proposed by Lear and Chisholm by taking the vibronic progression into consideration.[13] The characteristics of class IV, which may

be considered a subclass of class III, include the absence of (or minimal) vibronic coupling, and the solvent-independence of not only the IVCT but also the MLCT band.

The possibility to derive not only a general description of the principal electronic character of a system but also the crucial ET parameters from spectroscopic observables based on the well-known equations of the Marcus-Hush and Mulliken-Hush theories using two-state models or their extension to a three-state scenario (including bridge states in the latter case) has made the description of MV systems in terms of the Robin-Day classes almost universal in the field.[9-11,14,15] By also adding information on vibronic coupling, reasonably detailed descriptions of the ET characteristics can be derived from the IVCT band. While the IVCT transition typically appears as the lowest-energy transition in the NIR region for organic MV systems, the determination of the IVCT band within the NIR band envelope is more complicated in transition metal complexes, not only due the effects of solvent dynamics that characterize complexes in class II/III and near the class II-class III borderline, but also to the potential presence of additional electronic transitions of similar energy (e.g. localized d-d or inter-configurational bands).[3] The potential for multiple electronic transitions of similar energy but different electronic origin, together with the asymmetric IVCT band-shapes that characterize strongly coupled MV systems, renders derivation of the ET characteristics and electronic structure from NIR spectra alone very difficult in many MV transition-metal complexes, despite the popularity of such analyses.

In addition to solvent dynamics and internal vibrational modes, conformational effects within the molecular framework can also play a part in determining the optoelectronic properties of a MV complex. For example, in the case of the polyynediyl-bridged class III MV diruthenium complex $[\{Ru(PPh_3)_2Cp\}_2(\mu-C\equiv CC\equiv C)]^+$, a high-energy shoulder on the primary IVCT band is observed which cannot be accounted for easily by models that are based on the lowest energy conformation. Whilst the electronic structure of $[\{Ru(PPh_3)_2Cp\}_2(\mu-C\equiv CC\equiv C)]^+$ is well described in terms of a delocalized (Class III) electronic structure across the conformational space, the additional transition, which has appreciable MLCT character, gains intensity only for certain mutual orientations of the redox centers.[16] The identification of these conformational factors prompt

reconsideration of other ligand-bridged bimetallic mixed-valence complexes [M-bridge-M]$^+$ in which d-π-d overlap along the molecular backbone can be anticipated to be strongly dependent on the relative orientation of the constituent fragments.

A quantum-chemical methodology that gives a faithful description of localization/delocalization (see below),[16-21] has been used here to reconsider the description of three formally mixed-valence bimetallic ruthenium complexes for which a wealth of experimental data has been accumulated (Chart 1). The organometallic complexes [{Ru(dppe)Cp*}$_2$(μ-C$\equiv$CC$_6$H$_4$C$\equiv$C)]$^+$, [1]$^+$, and [{*trans*-Ru(dppe)$_2$Cl}$_2$(μ-C$\equiv$CC$_6$H$_4$C$\equiv$C)]$^+$, [2]$^+$ both contain the 1,4-diethynylbenzene (μ-C$\equiv$CC$_6$H$_4$C$\equiv$C) bridge but differ in the composition of the supporting ligands, and in both cases, conflicting evidence exists regarding the MV classification.[22,23] For comparison purposes, the classical coordination complex, the Creutz-Taube ion,[6,7,24] [3]$^{5+}$, for which the intermediate class II/III was originally coined,[3] has also been studied using the same methods. Whilst a number of the principal spectroscopic features are reproduced by calculations based on the lowest energy conformation, the optical *and* vibrational spectra of [1]$^+$ and [2]$^+$ (Figure 2) are better modeled by a series of structures that account for a distribution of relative conformations of bridge and redox centers in solution. The thermal population of a conformational phase space encompassing both localized and delocalized charge distributions limits the usefulness of a description of such complexes in terms of a single, static Robin-Day class. A more accurate explanation of the spectroscopic properties and electronic characteristics requires consideration of the internal rotational dynamics of the molecule and description in terms of a continuum of class II and class III states rather than a specific single class.
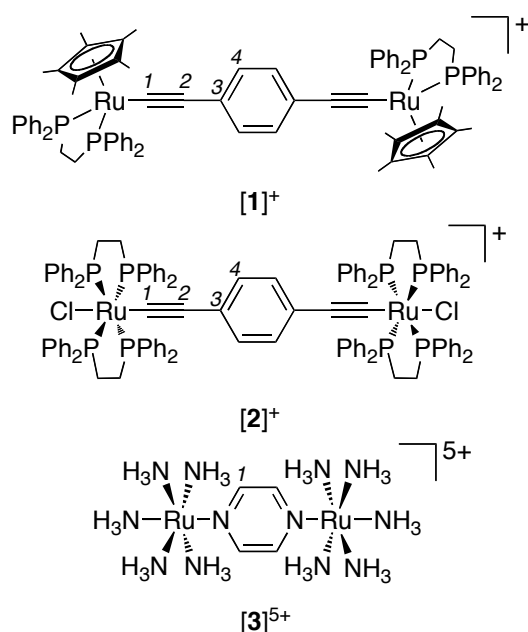
Chart 1. Mixed-valence diruthenium cations.

Computational Details.

Calculations have been carried out on the full complexes $[\mathbf{1}]^+$, $[\mathbf{2}]^+$, and $[\mathbf{3}]^{5+}$, and in case of $[\mathbf{1}]^+$ and $[\mathbf{2}]^+$ also on truncated models $[\mathbf{1\text{-}Me}]^+$ and $[\mathbf{2\text{-}Me}]^+$, where the phenyl substituents in the dppe ligands were replaced by methyl groups (i.e dmpe ligands). This allowed us to examine larger portions of the conformational space at reduced computational cost. All calculations have been performed using a version of the TURBOMOLE 6.4[25] code locally modified by the Berlin group. For selected cases, additional single-point TDDFT calculations were carried out using the Gaussian09 code,[26] which features a somewhat different treatment of the solvent model for excitations.[16,20] The computational protocol used, which has been developed specifically to provide accurate ground- and excited-state properties for organic[17-21] and transition-metal[16] mixed-valence systems, is based on the adjusted global hybrid functional BLYP35,[17]

$$E_{XC} = 0.65(E_X^{LSDA} + \Delta E_X^{B88}) + 0.35 E_X^{exact} + E_C^{LYP}$$

in conjunction with polarizable continuum solvent models. While not a thermochemically optimized functional, BLYP35 has been shown to provide a good balance between reduced self-interaction errors and a simulation of static correlation. Although other functionals like the BMK global hybrid[27] or the CAM-B3LYP range

6

hybrid[28] have been found to provide a similar balance between localization and delocalization as BLYP35, these are not available in the Turbomole code used in this study.[19,20] Experimental measurements of the UV-vis-NIR and IR spectra of [**1**]$^+$ and [**2**]$^+$ were carried out using samples generated by one-electron oxidation of **1**[22] and **2**[29] in a spectroelectrochemical cell[30] from dichloromethane (DCM; permittivity $\varepsilon = 8.93$) solutions containing 0.1 M NBu$_4$BF$_4$ supporting electrolyte. Spectroscopic data from [**3**][PF$_6$]$_5$ in acetonitrile (MeCN, $\varepsilon = 37.64$) were taken from the literature.[24] In the computational work, these solvents were considered by the conductor-like-screening solvent model (COSMO)[31] (and by the closely related C-PCM model[32,33] in the Gaussian09 TDDFT calculations). Notably, the TDDFT calculations took into account non-equilibrium solvation.[34,35]

For all calculations, split-valence basis sets def2-SVP on the lighter atoms and the associated Stuttgart effective-core potentials with a corresponding def2-SVP valence basis for ruthenium were employed.[36-38] Calculated harmonic vibrational frequencies were scaled by an empirical factor of 0.95.[39,40] Spin-density and molecular orbital plots were obtained using the Molekel program.[41]

For [**1-Me**]$^+$, a two-dimensional relaxed scan of the potential-energy surface (PES) with a fixed P-Ru-Ru-P dihedral angle Ω (which defines a dihedral angle between the half-sandwich metal complex end groups) and a fixed P-Ru-C$_3$-C$_4$ dihedral angle Θ_{real} (dihedral between bridge and a selected end group) was performed (Figure 2). Starting from a C_i-symmetric structure, both dihedral angles were varied in steps of 10°, from 180° to 0° for Ω and from +50° to −100° for Θ_{real}, to cover a reasonable phase space of the relative conformation of the Ru fragments, and of the phenylene moiety in the bridging ligand. In the lowest-energy structures, which are found at $\Omega = 180°$ and $\Omega = 0°$ and correspond to *transoid* and *cisoid* forms of the complex, the plane of the phenylene moiety in the bridge bisects the P-Ru-P angle in each of the diphosphine chelate ligands. In these two structures, the P-Ru-C$_3$-C$_4$ dihedral angle Θ_{real} of ca. 41° (Figure 2) can be translated into an effective X-Ru-C$_3$-C$_4$ dihedral angle Θ_{eff} of 0°, where X is the midpoint between the two phosphorus atoms of the chosen diphosphine ligand. As Θ_{eff} gives a somewhat more intuitive picture of the relative conformations (Figure 2), we have transformed Θ_{real} to Θ_{eff} for the entire relaxed scan and will discuss results predominantly based on conformations defined in terms of Θ_{eff}. A perpendicular arrangement of the phenylene plane relative to the

chelate ligands thus translates from a Θ_{real} near $-50°$ to a Θ_{eff} of ca. $+90°$ (Figure 2). Due to small variations in the remaining degrees of freedom throughout the scan and due to the reduced symmetry of the system along the scan profile, Θ_{eff} may deviate by some fraction of a degree from idealized values at the special points. For [**2-Me**]$^+$, a similar scan has been restricted to a somewhat smaller range of end-group and bridge dihedral angles ($0° \leq \Omega \leq 90°$ and $-50° \leq \Theta_{real} \leq +50°$, i.e. $-8.3° \leq \Theta_{eff} \leq +92.2°$), reflecting the higher local symmetry of the ligand environment (C_{2v}) at the ruthenium centers.

Due to the even higher local symmetry of the coordination sphere in the Creutz-Taube ion [**3**]$^{5+}$ (C_{4v}), the phase space necessary to be covered explicitly was smaller ($0° \leq \Omega \leq 45°$ and $0° \leq \Theta_{eff} \leq 45°$) and was surveyed in $5°$ steps. Here Ω is the N_{eq}-Ru-Ru-N_{eq} dihedral angle and $\Theta_{eff} = 0°$ corresponds to the pyrazine plane bisecting the angle between two equatorial amine ligands. The resulting data were interpolated using the MATLAB griddata method 4 to construct the PES plots.[42] For crucial points on the obtained PES, selected minimum and transition state structures were subsequently reoptimized without constraints.
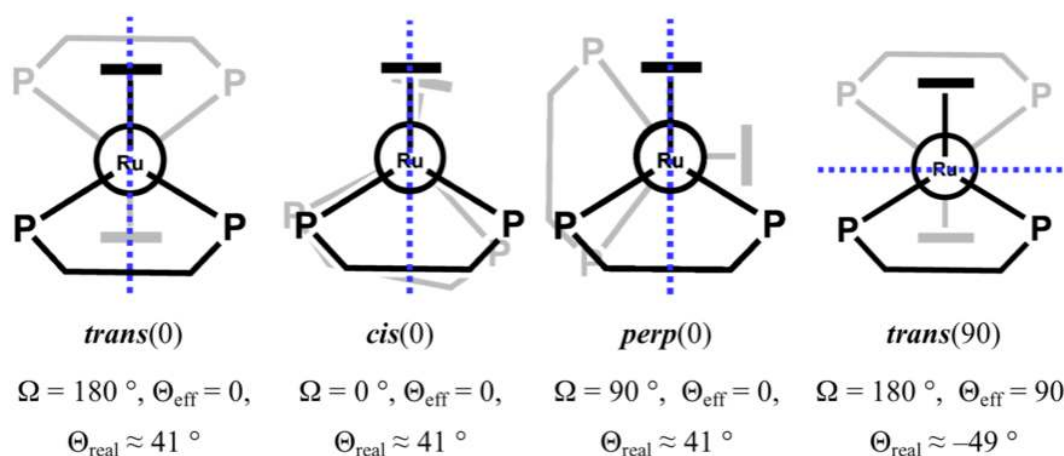

trans(0)
$\Omega = 180°, \Theta_{eff} = 0,$
$\Theta_{real} \approx 41°$

cis(0)
$\Omega = 0°, \Theta_{eff} = 0,$
$\Theta_{real} \approx 41°$

perp(0)
$\Omega = 90°, \Theta_{eff} = 0,$
$\Theta_{real} \approx 41°$

trans(90)
$\Omega = 180°, \Theta_{eff} = 90,$
$\Theta_{real} \approx -49°$

Figure 2. Schematic relative orientation of the metal redox centers (black and grey) and the bridge phenyl plane (dashed blue) of [**1-Me**]$^+$ (similar values hold for [**2-Me**]$^+$).

For each point on the PES created in this way, single-point TDDFT calculations were performed. The results are displayed graphically not only as stick spectra, but were additionally convoluted with Gaussian broadening ($\sigma = 300$ cm^{-1}, full width at half maximum FWHM = 706.4 cm^{-1}) using the Q-Spector program previously designed for IR spectra,[43] for better comparison with the experimental spectra. To

take into account the thermal population of different parts of the considered conformational space, the computed data from all points were combined in one spectrum, based on weighting of the computed intensities by a Boltzmann factor $e^{-\Delta E/k_B T}$, where ΔE is the energy relative to the most stable conformer (e.g. $\Omega = 180\,°$ and $\Theta_{eff} = 1.7\,°$ for [**1-Me**]$^+$), k_B is the Boltzmann constant, and T was set to 298.14 K to correspond to the room-temperature experimental conditions.

Results and Discussion

Analysis of [1]$^+$. Fox et al. have recently reported the appearance of the IR and NIR spectra of [**1**]$^+$ (Figure 3).[22] The number and energy of $\nu(C\equiv C)$ vibrational modes together with the shape of the NIR absorption envelope was proposed to be due to thermal population of a range of conformers with distinct (localized / delocalized) electronic character. These observations could not be corroborated by the B3LYP/3-21G* calculations performed on a single conformation using simplified molecular models.[22] However, whilst B3LYP is capable of modeling molecules with delocalized electronic structures quite well, in general density functionals with low exact-exchange admixture are less well suited to the description of class II situations close to the border between class II and class III, due to extensive delocalization errors.[17,20] Moreover, in the experimental systems, charge distribution is likely biased by the solvent polarity and interactions with the counter-ion; in order to accurately model these situations computational models must also adequately address the nature of the medium.
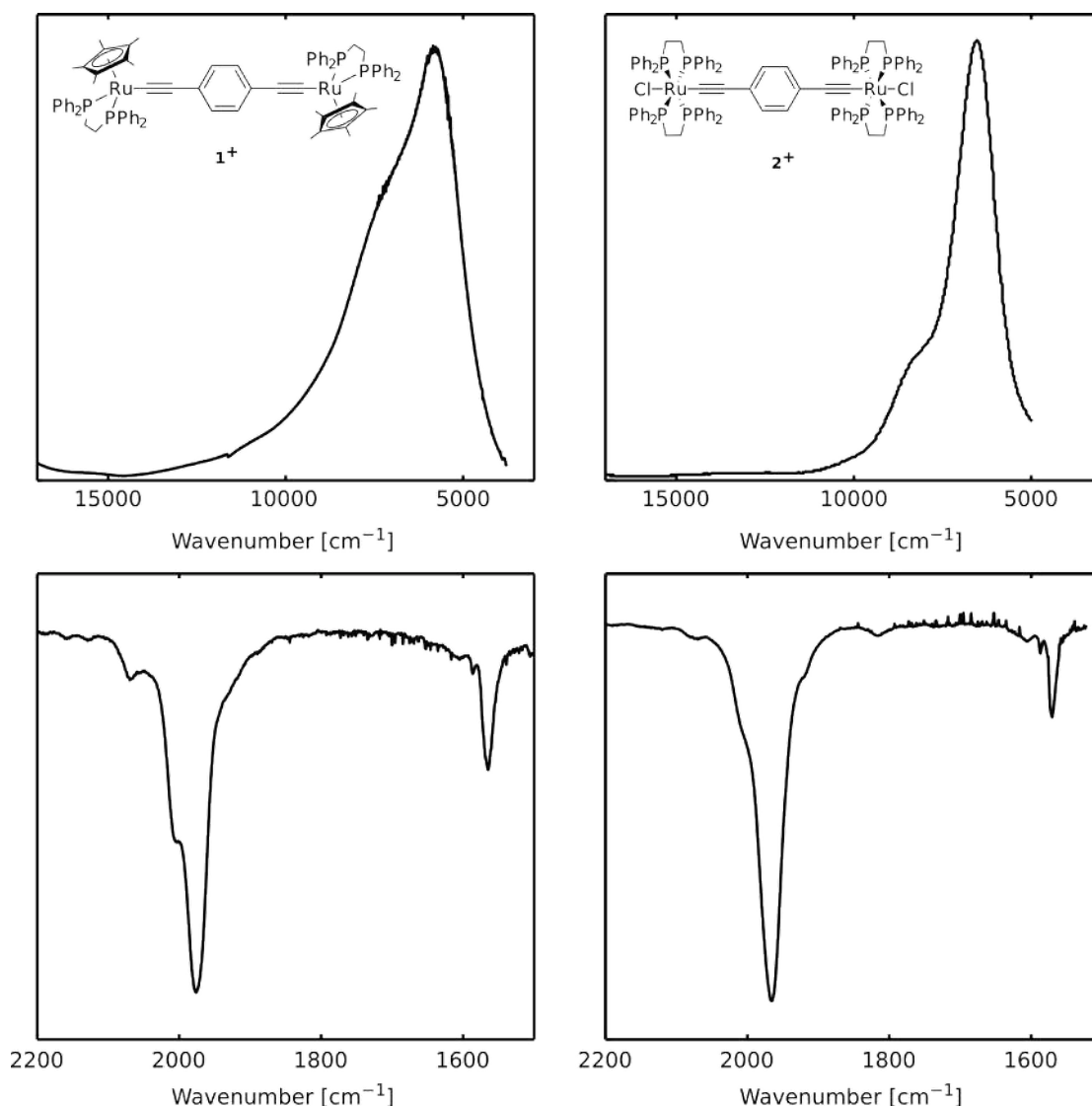
Figure 3. The spectroelectrochemically generated NIR (upper) and IR (lower) spectra of [**1**]$^+$ (left)[22] and [**2**]$^+$ (right) in DCM / 0.1 M NBu$_4$BF$_4$

To better model [**1**]$^+$, a computational protocol that a) uses a functional that is well-balanced regarding delocalization errors and dynamical/nondynamical correlation, and b) includes at least dielectric solvent effects throughout the entire computational procedure should be employed. Such a protocol (see Computational Details) has recently been introduced for organic MV systems, where it has allowed valid descriptions close to the class II – class III borderline for a wide variety of MV systems and solvent environments.[17-21] Still more recently, it has been extended to applications in the modeling of ET processes in transition-metal MV systems.[16] However, regardless of the computational methodology employed, any interpretation of quantum chemical results based on a single, static, lowest-energy molecular structure will not accurately model systems in which molecular dynamics play an

important role on the optoelectronic properties of a molecule. These points are illustrated further below.
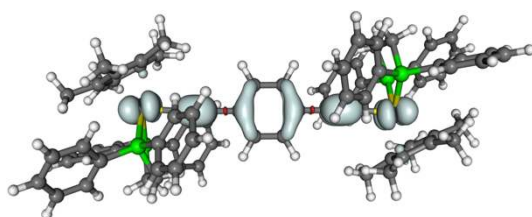

Figure 4. Spin-density isosurface plot (± 0.002 a.u.) of *trans*-[**1**]$^+$.

Full BLYP35/def2-SVP/COSMO(DCM) structure optimization of [**1**]$^+$, starting from a C_i-symmetric input, gave a delocalized (class III) structure with a trans-arrangement of the two redox centers, denoted *trans*-[**1**]$^+$ (c.f. Figure 2). The spin-density in *trans*-[**1**]$^+$ (Figure 4) is evenly distributed over the molecular backbone with both the bridging ligand (C≡C / C_6H_4 / C≡C 19 % / 18 % / 19 %) and the metal centers, Ru(dppe)Cp*, (21 % / 21 %) contributing significantly (the large involvement of the bridge atoms in carrying the spin density supports redox non-innocent description of this ligand in such delocalized arrangements[44,45]). This solution corresponds to lowest-energy states calculated previously for [**1**]$^+$ and analogues.[22,46] The symmetrical class III situation is further supported by a negligible dipole moment ($\mu = 0.0$ D), and by the computed single harmonic ν(C≡C) vibrational frequency at 1978 cm^{-1} (scaled by 0.95, see Computational Details), which compares well with the very strong band at 1974 cm^{-1} in the experimental spectrum (Figure 3). TDDFT calculations with *trans*-[**1**]$^+$ at the same computational level gave a single, very intense ($\mu_{trans} = 17.5$ D) NIR transition at 6566 cm^{-1}, in good agreement with the most intense peak at 5750 cm^{-1} in the experimentally determined spectrum of [**1**]$^+$ (even better agreement is obtained with the slightly different CPCM solvent implementation in the Gaussian 09 program, cf. Table S2 in Supporting Information). This excitation largely corresponds to a β-HOMO to β-SOMO transition which has substantial bridge π–π* character (Figure 5). However, the additional features at the high-energy side of the experimental NIR band cannot be explained from the TDDFT results.

Several models for mixed-valence complexes have been described which can account for the appearance of multiple transitions of similar energy to the IVCT transition predicted from the Marcus-Hush two-state model. In the case of localized

MV complexes towards the class II-III boundary, Meyer and colleagues have shown that the combination of low symmetry, substantial metal-bridge orbital overlap and the use of heavy metals with high spin orbit coupling constants (e.g. Os(III), $\xi \sim 3000$ cm^{-1}) can lead to the appearance of three IVCT and two $d\pi \rightarrow d\pi$ transitions through the lifting of parity or LaPorte rules. In the case of lighter metals such as Ru(III) the lower spin orbit coupling constant ($\xi \sim 1000$ cm^{-1}) not only serves to shift the $d\pi \rightarrow d\pi$ transitions to lower energy (e.g. into the IR region), but also decreases the energy difference between the distinct IVCT transitions leading to a broad NIR absorption feature comprised of the overlapped bands.[3] Alternatively, extension of the two-state model by explicitly including both symmetric *and* asymmetric vibrational mode and addressing explicitly the bridge orbitals as a mediating state for electron transfer (three-state model) and multiple d-electrons (four-state model) is useful in accounting for the observation of one or more MLCT/LMCT transitions in addition to the IVCT band in more weakly coupled MV systems and the pronounced asymmetry of these bands strongly coupled (Class III) systems.[15]

However, each of these frameworks assumes that the molecular system under investigation can be placed into one of the expanded Robin-Day classes, and analysis or fitting of the spectroscopic data is used to extract the underlying electronic coupling information. Given the subtle distinctions that can arise from different treatments of the NIR spectra under localized (class II or II/III) or delocalized (class III or IV) regimes, the accurate interpretation of the electronic absorption data often requires supporting evidence for the time-scale of the electron-transfer event or delocalization. To this end, the observation or absence of IR active modes from both the supporting ligands on the metal centers and the bridging ligand itself is often critical in determination of the choice of method of analysis.

In the present cases of [**1**]$^+$ and [**2**]$^+$ the interpretation of the NIR spectra (Figure 3) in terms of a series of overlapping IVCT transitions and a formally Ru(II/III) d^6/d^5 MV system (at or near the Class II/III borderline) might account for the overlapping transitions that comprise the NIR band envelope, either in terms of multiple IVCT transitions or the presence of closely lying MLCT/LMCT transistions. However, the IR spectra are difficult to reconcile with this interpretation. For example, in the case of [**1**]$^+$, whilst the $\nu(C \equiv C)$ bands at 2061, 1915 cm^{-1} and the phenylene ring $\nu(CC)$ band at 1564 cm^{-1} are consistent with a localized MV structure, the $\nu(C \equiv C)$ bands at

1997 and 1974 cm^{-1} are not easily accounted for in terms of a localized model. Similar points apply to the spectra of [**2**]$^+$ (Figure 3). Although a more strongly coupled (delocalized) model might be more consistent with these latter ν(C≡C) IR bands, the three-state model predicts only an IVCT transition with an asymmetric band shape arising from the low energy 'cut-off' whilst the four-state model predicts a significant energy difference between the IVCT and the only MLCT transition with appreciable intensity. Indeed, the IR spectra are inconsistent with the various arguments that can be put forward based solely on the appearance of the NIR bands for assignment of [**1**]$^+$ and [**2**]$^+$ to any one of the conventional Robin-Day classes II, II/III or III.
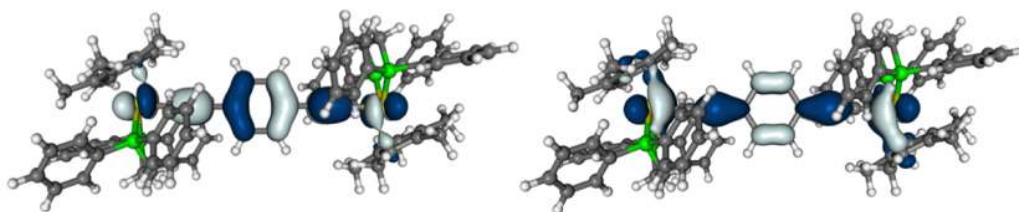

Figure 5. Isosurface plots (± 0.03 a.u.) of the β-SOMO (left) and β-HOMO (right) of ***trans*-[1]**$^+$.

Given the importance that different molecular conformations play in the appearance of the UV-vis-NIR spectrum of the related complex [{Ru(PPh$_3$)$_2$Cp*}$_2$(μ-C≡CC≡C)]$^{+}$,[16] we proceeded to a full 2D relaxed scan (BLYP35/def2-SVP/COSMO(DCM) level) of metal fragment and bridge conformations for the truncated model [**1-Me**]$^+$ (see Computational Details). Two minima on this 2D PES were initially identified (Figure 6). These minima are almost isoenergetic, and correspond to the *trans* ($\Omega \approx 180°$, $\Delta E = 0.0$ kJ/mol) and the analogous *cis* ($\Omega \approx 0°$, $\Delta E = 0.1$ kJ/mol) orientations of the ruthenium fragments. In both of these minima, the bridge phenyl plane bisects the two P-Ru-P angles of the diphosphine ligands (i.e. $\Theta_{eff} \approx 0$ °) and hence are denoted ***trans*(0)-[1-Me]**$^+$ and ***cis*(0)-[1-Me]**$^+$. These two structures provide optimal overlap between the bridging ligand π-system and the metal d orbitals of similar symmetry and hence the strongest electronic coupling of the two redox centers. Consequently the *cis* minimum ***cis*(0)-[1-Me]**$^+$ also features almost symmetrical structural parameters and an even distribution of the spin-density

over the molecular backbone (Figure 7), in a manner very similar to that described above for the *trans* structure. The apparent third minimum on the upper side ($\Omega \approx 40°$; $\Theta_{eff} \approx 140°$) of Figure 6 is only part of the trough of a minimum equivalent to ***cis***(0)-[**1-Me**]$^+$. However, the full optimizations without constraints furnished a third, very shallow minimum that is not apparent from data presented in Figure 6 for the model system [**1-Me**]$^+$**,** and which will be discussed further below.

Figure 6 shows that, as expected, rotation of the phenylene moiety in the bridge relative to the metal centers (i.e. Θ_{eff}) has a larger impact on the energy of the system than rotation of the metal end groups relative to each other (i.e. Ω). Maxima occur for $\Theta_{eff} \approx 90°$ at $\Omega \approx 180°$ and $\Omega \approx 0°$. Due to the perpendicular orientation of the phenylene moiety in these higher-energy model structures (with respect to the mirror plane bisecting the P-Ru-P angle in the Ru(PP)Cp moiety), electronic coupling is reduced, and the spin-density distribution exhibits partial symmetry breaking towards one of the metal centers (Figure 7). The symmetry breaking is also apparent from key structural parameters such as the difference in the Ru-C≡C bond lengths for the two halves $\Delta d(Ru-C_1)$ of some 0.03 Å for both maxima. Indeed, most points with perpendicular bridge orientation ($\Theta_{eff} \approx 90°$) correspond to localized spin-density distributions (see Supporting Information Figure S1, Figure 7c, Figure 7d and Figure 8a). However, the highest-energy maximum occurs at only ca. 28.6 kJ/mol above the lowest-energy minimum, and most regions are at much lower energy. Figure S1 in the Supporting Information illustrates the progressive localization of the spin-density as $\Theta_{eff} \rightarrow 90°$ for $\Omega = 180°$ (i.e. rotation of the bridge) a process that is accompanied by a dramatic reduction of the bridge contributions to the spin-density (within the bridging ligand only the C≡C unit close to the oxidized metal center always bears a significant share of the spin). That is, as the phenylene ligand rotates around the long molecular axis, [**1-Me**]$^+$ and hence by inference [**1**]$^+$ shifts from strongly coupled class III situations with large bridge contributions for structures with $\Theta_{eff} = 0°$ towards more weakly coupled class II situations with $\Theta_{eff} \approx 90°$. As the energy penalty associated with this rotation is so small, the entire conformational phase space is sampled at room temperature.
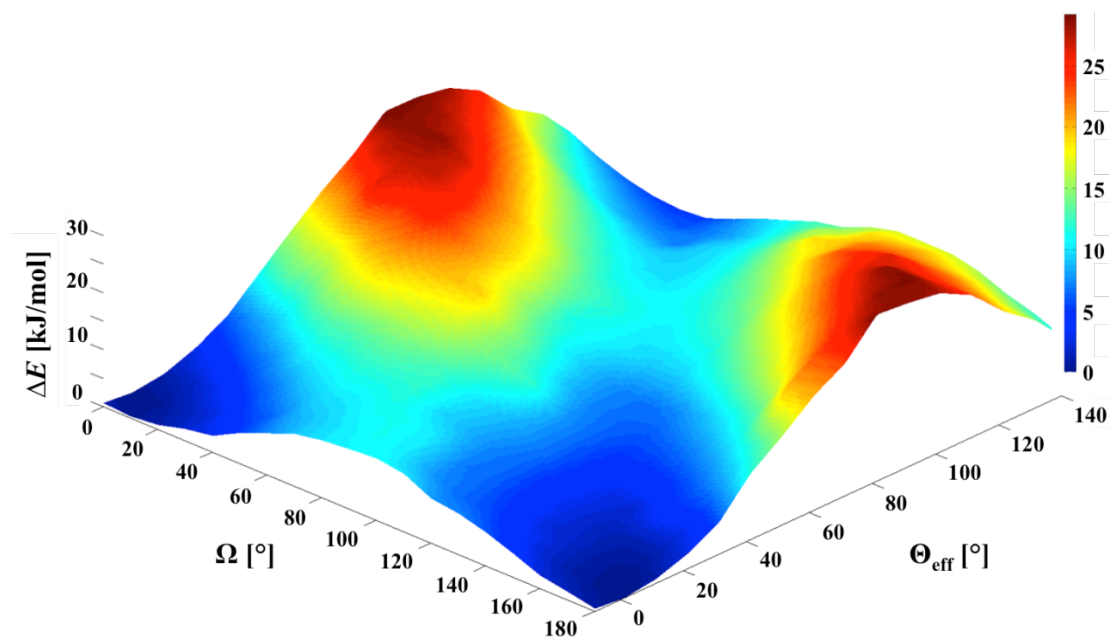
Figure 6. Computed potential energy surface of [**1-Me**]$^+$ (BLYP35/def2-SVP/COSMO(DCM) level).

The relative orientation of the metal fragments, defined by dihedral angle Ω, also influences the distribution of spin-density over the molecular framework, and hence the most appropriate Robin-Day classification at each point on the 2D PES: keeping $\Theta_{eff} \approx 0°$ and rotating the end groups to a perpendicular orientation ($\Omega \approx 90°$) leads to a low-energy ridge (below 15 kJ/mol; Figure 6). The perpendicular orientation of the end groups also diminishes the electronic coupling to an extent that the charge may become localized (Figure 7d, Figure 8a).

It is worth noting at this point that one-dimensional cuts through the energy profile at either $\Omega \approx 0°$ or 180°, and also through $\Theta_{eff} \approx 0°$ superficially resemble the shape of the double-well ground-state potential in the two-state model of a class II system. Despite the apparent similarity there is a fundamental difference: here the minima correspond to delocalized class III situations, whereas the spin-density becomes more and more localized upon approaching $\Omega = 90°$ or $\Theta_{eff} = 90°$ (Figure 6, Figure 7, Figure 8a).

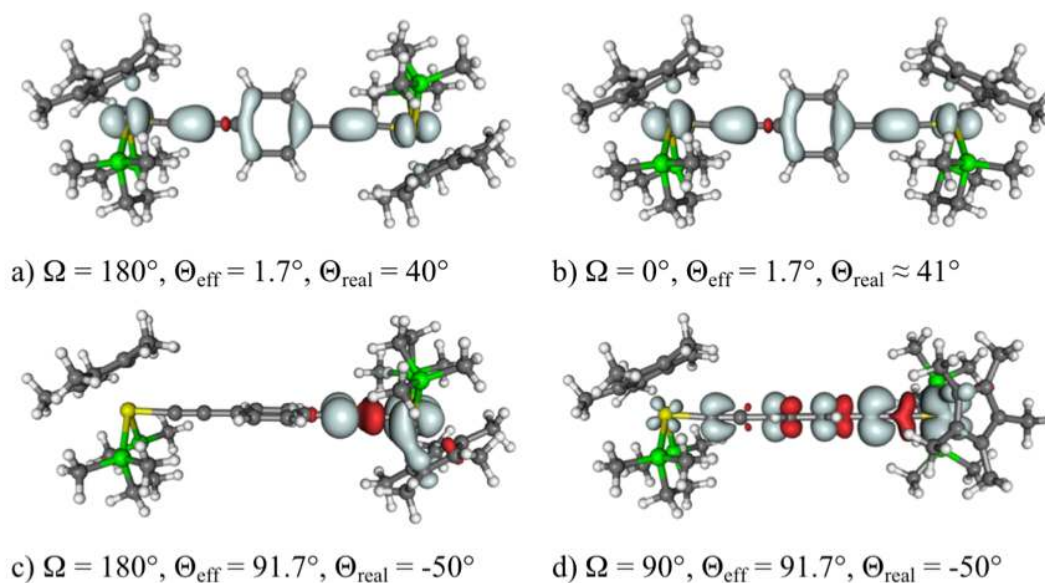a) $\Omega = 180°$, $\Theta_{eff} = 1.7°$, $\Theta_{real} = 40°$ b) $\Omega = 0°$, $\Theta_{eff} = 1.7°$, $\Theta_{real} \approx 41°$

c) $\Omega = 180°$, $\Theta_{eff} = 91.7°$, $\Theta_{real} = -50°$ d) $\Omega = 90°$, $\Theta_{eff} = 91.7°$, $\Theta_{real} = -50°$

Figure 7. Spin-density isosurface plots (± 0.002 a.u.) of [**1-Me**]$^+$ for different points on the PES (BLYP35/def2-SVP/COSMO(DCM) level; cf. Figure 3 for the definition of dihedral angles and Figure 6 for the PES).

The two conformational minima found in the relaxed scan for [**1-Me**]$^+$ (Figure 6) have been fully reoptimized (BLYP35/def2-SVP/COSMO(DCM) level), initially for the truncated complex [**1-Me**]$^+$ (with dmpe ligands) and subsequently for the full complex [**1**]$^+$ (with dppe ligands), with comparable results. The energies of the lowest-energy minima for the truncated system, ***trans*-[1-Me]$^+$** and ***cis*-[1-Me]$^+$** differ by only 0.1 kJ/mol. However, the spin-densities in these fully optimized structures are not completely symmetrical (Table S3 in the Supporting Information) and whilst structural symmetry breaking is moderate the differences are sufficiently small that the electronic character is probably still in line with a class III situation (differences in the Ru-C$_1$ bond lengths are 0.014 Å for ***cis*-[1-Me]$^+$** and 0.015 Å for ***trans*-[1-Me]$^+$**).
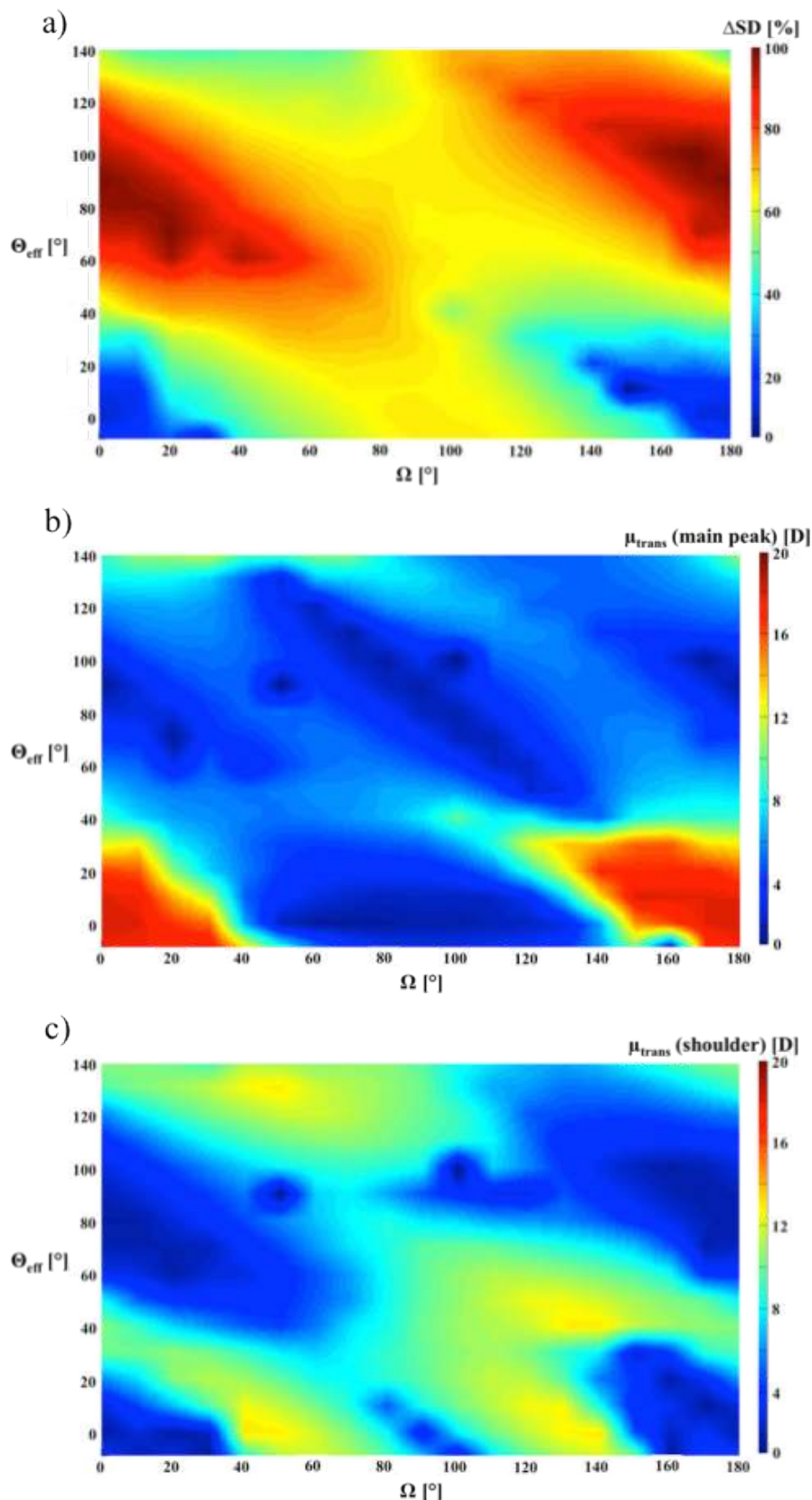
16

a)

b)

c)

Figure 8. Properties (BLYP35/def2-SVP/COSMO(DCM) level) as function of conformational phase space of [**1-Me**]$^+$. a) Color plot of Mulliken spin-density differences, ΔSD, between the two Cp*(dmpe)Ru-C≡C units. 0 % indicates fully delocalized and 100 % fully localized distributions (top). b) TDDFT transition dipole moment μ_{trans} of the main π→π* excitation at around 6000 cm^{-1} (middle). c) TDDFT transition dipole moment of the IVCT excitation at higher energies 7350-9450 cm^{-1}

17

(bottom). For $\Omega = 50°$, $\Theta_{eff} = 91.7°$ and for $\Omega = 100°$, $\Theta_{eff} = 101.6°$, TDDFT did not converge, and the values were set to 0 ("holes").

A third, very shallow minimum (indicated by the absence of imaginary frequencies) with perpendicular orientation of the end groups ($\Omega = 90°$, $\Theta_{eff} = 0°$), corresponding to the low-energy ridge in Figure 6 (10.4 kJ/mol above the lowest-energy minimum *trans*-[**1-Me**]$^+$) was also identified. Compared to this minimum energy structure, the energy goes slightly up when fixing $\Omega = 85°$ or $\Omega = 95°$, and the structure remains a minimum when improving the integration grid (multiple grid m5[47]) and when using tighter structure optimization criteria. While this is certainly only a short-lived metastable structure, consideration of such extra minima will be useful for the interpretation of the IR features (see below). This extra minimum exhibits a localized spin-density (Table S3 in Supporting Information) and the structural features of a class II system ($\Delta d(Ru-C_1) = 0.046$ Å), and it is denoted *perp*-[**1-Me**]$^+$.

Full optimization for the non-truncated complex [**1**]$^+$ afforded the same three minima, *trans*-[**1**]$^+$ (already discussed above), *cis*-[**1**]$^+$, and *perp*-[**1**]$^+$, each of very similar energy (*cis*-[**1**]$^+$ and *perp*-[**1**]$^+$ are 0.1 kJ/mol and 7.5 kJ/mol, respectively, above *trans*-[**1**]$^+$). The spin-density distributions (Table S3 in Supporting Information) and structures of *trans*-[**1**]$^+$ ($\Delta d(Ru-C_1) = 0.002$ Å) and *cis*-[**1**]$^+$ ($\Delta d(Ru-C_1) = 0.005$ Å), are notably more symmetric than for the truncated complex, in agreement with clear class III behavior, whereas the third, metastable minimum, *perp*-[**1**]$^+$, remains clearly localized (with a slightly larger bridge contribution than *perp*-[**1-Me**]$^+$; Table S3). Together, these results suggest a somewhat stronger electronic coupling between the redox centers for the full system (perhaps due to the relatively greater electron donating properties of dmpe ligands favoring more metal-based redox character and a greater energetic mismatch with the bridging ligand orbitals) but an overall very similar situation regarding the conformational profiles of [**1**]$^+$ and [**1-Me**]$^+$. This is a useful point to note for future studies of related systems with a view to managing computational effort.

The population of low-energy regions on the PES which feature molecular structures with delocalized to localized electronic characteristics is expected to heavily influence the appearance of the NIR spectrum of [**1**]$^+$ at ambient temperatures. This proposal has been tested by TDDFT calculations (BLYP35/def2-

18

SVP/COSMO(DCM) level) for a large subset of points (a restriction to $0° \leq \Theta_{eff} \leq 90°$ is justified due to approximate symmetry relations) on the 2D PES of [**1-Me**]$^+$ (cf. Figure 6). Figure 9 combines the Boltzmann-weighted superposition (cf. Computational Details) of the stick spectra (red) for all points sampled, with the experimental band profile for [**1**]$^+$. Additionally, the stick spectra have been convoluted with Gaussian functions ($\sigma = 300$ cm^{-1}, full width at half maximum FWHM = 706.4 cm^{-1}; grey shaded area). While being aware that Gaussian broadening and neglect of vibronic effects is not fully adequate, particularly for the low-energy side of the band,[1,15] agreement with the band shape at the high-energy side is encouraging (also given the use of a truncated model). The computed high-energy shoulder is less intense than in the experimental spectrum but at the correct position relative to the main band maximum (c.f. Figure 3, Figure 9). This may be due to the insufficient description of the band asymmetry of the main absorption, which would lead to a broader and "flatter" main feature, a more pronounced overlap between the bands of the CT and $\pi-\pi^*$ excitation and thus to a higher shoulder.
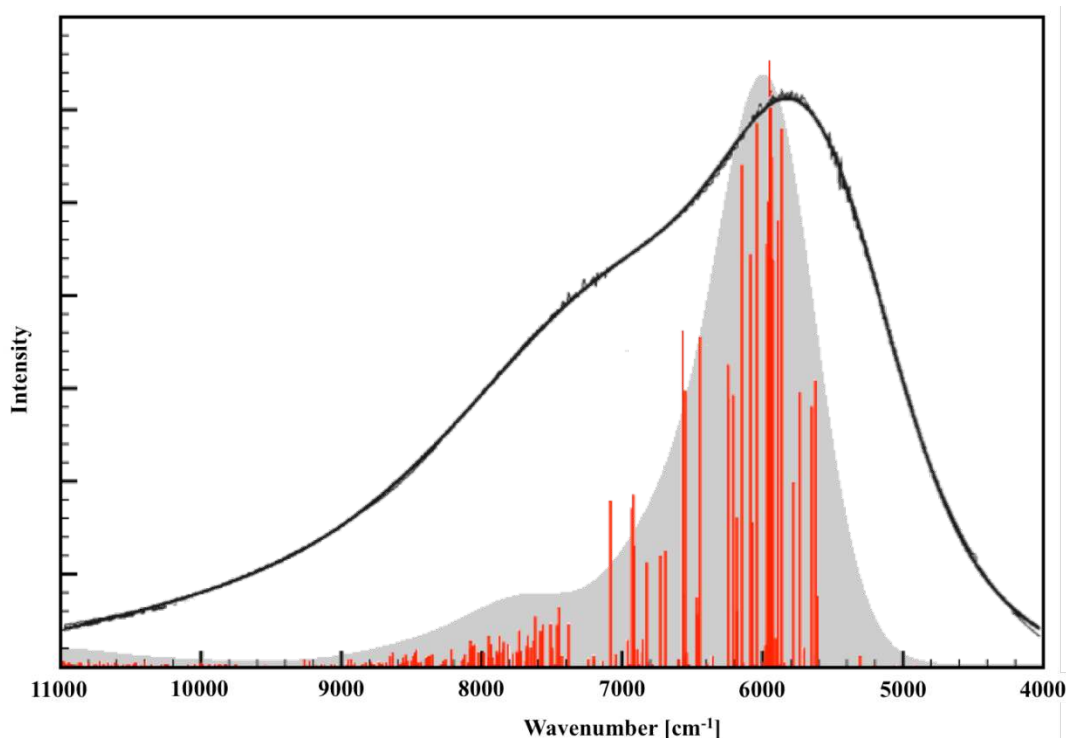

Figure 9. Computed Boltzmann-weighted TDDFT stick spectra (red) with Gaussian broadened envelope ($\sigma = 300$ cm^{-1}, FWHM = 706.4 cm^{-1}, grey) for [**1-Me**]$^+$ compared to experimental IVCT band[22] (black) of [**1**]$^+$.

The contributions from different parts of the conformational PES to the NIR spectral band shape are further analyzed in Figure 8. The differences in the Mulliken

spin-densities on the two metal fragments (Figure 8a) show that delocalized class III behavior is concentrated around the *cis*(0)-[**1-Me**]$^+$ and *trans*(0)-[**1-Me**]$^+$ minima. Structures in these areas give rise to the transitions that dominate the main NIR absorption near 6000 cm^{-1} (Figure 8b). The electronic coupling between the metal centers is weakest, and thus the localization most pronounced (Figure 8a) near the energy maxima at $\Omega = 180°$, $\Theta_{eff} = 90°$ and $\Omega = 0°$, $\Theta_{eff} = 90°$ (cf. Figure 6). These fully localized structures give rise to more intense excitations around 3500 cm^{-1} and above 12000 cm^{-1} and do not contribute to the band shoulder around 8000 cm^{-1} (Figure 8c, Figure 9). The higher energy shoulder observed in the experimental spectrum arises from sections on the PES (yellow peaks in Figure 8c) that feature only partly localized spin-densities (green areas in Figure 8a), but it may nevertheless be viewed as an IVCT band with considerable MMCT character. For structures in which the redox centers are nearly perpendicular and the bridge bisects one of the P-Ru-P angles, a third intense excitation arises (Figure S2), which corresponds to an IVCT transition and is very close in energy to the previously discussed IVCT excitation and thus contributes to the shoulder as well.

The TDDFT results for the fully optimized minimum structures of the truncated system [**1-Me**]$^+$ may be used to illustrate these aspects further: starting with the truncated system, conformer *trans*-[**1-Me**]$^+$ contributes only one intense transition in the NIR region, at 6108 cm^{-1} ($\mu_{trans} = 17.7$ D) with considerable diethynyl benzene π-π* character. Similarly *cis*-[**1-Me**]$^+$ has only one intense transition at 6085 cm^{-1} ($\mu_{trans} = 17.8$ D). Clearly these "class III" areas of the PES are responsible for the main feature in the NIR spectrum. In contrast, *perp*-[**1-Me**]$^+$ features one intense transition at 9849 cm^{-1} ($\mu_{trans} = 9.0$ D) and three lower-intensity transitions at 9334 cm^{-1} ($\mu_{trans} = 4.2$ D), 10196 cm^{-1} ($\mu_{trans} = 5.9$ D) and 14508 cm^{-1} ($\mu_{trans} = 2.5$ D); the first three transitions are consistent with absorptions that give rise to the shoulder area.

The TDDFT results for the full system [**1**]$^+$ give very similar excitations for the *trans* and *cis* conformers, systematically blue-shifted by ca. 400 cm^{-1} relative to the similar conformations of [**1-Me**]$^+$ (see Table 1 below for a summary), again with delocalized π-π* character (β-HOMO$\rightarrow\beta$-SOMO transition). The most pronounced differences occur for *perp*-[**1**]$^+$. The main transition appears at 9139 cm^{-1} ($\mu_{trans} = 10.6$ D) and arises mainly from the β-HOMO$\rightarrow\beta$-SOMO excitation (75 %),

with the β-HOMO–1→β-SOMO excitation also contributing (11 %). While the β-SOMO is mainly centered at one Cp*(dmpe)Ru-C≡C unit (64 %) and the aromatic part of the bridge (20 %), the β-HOMO and the β-HOMO–1 are localized on the opposite C≡C-Ru(dmpe)Cp* center (87 %, 78 % respectively), with little contribution from the phenyl ring (3 %, 7 % respectively) or the first ethynyl-metal part (0 %, 7 % respectively) (Figure 10). This transition thus exhibits significant charge-transfer character, but it involves the bridge somewhat more than for the truncated system. Overall symmetry breaking for this conformer is still notable but less pronounced than for the truncated complex (as noted above, the dmpe ligands appear to support somewhat more metal-localized redox character). Two further transitions between 9200 cm^{-1} and 20000 cm^{-1} are also computed. An excitation at 9412 cm^{-1} (μ_{trans} = 7.4 D) contains contributions both from β-HOMO–1→β-SOMO (71 %) and β-HOMO→β-SOMO (16 %) excitations. These are the same orbitals that contribute to the main transition, although to a reversed extent, and hence the transition also has charge-transfer character. Finally, a mixed β-HOMO–2→β-SOMO (78 %) and β-HOMO–1→β-SOMO (13 %) transition, again with CT contributions, is found at 14248 cm^{-1} (μ_{trans} = 2.3 D). Agreement of these excitations with the high-energy shoulder of the experimental IVCT band (Figure 3) is somewhat inferior compared to the truncated model. However, it should be noted that the determination of the experimental shoulder maximum has been based on a Gaussian fit that may well be inaccurate.[22] Moreover, the TDDFT excitation energies depend notably on the precise modeling of non-equilibrium solvation (as demonstrated by lower and thus more accurate excitation energies obtained with Gaussian 09, cf. Table S2 in Supporting Information).
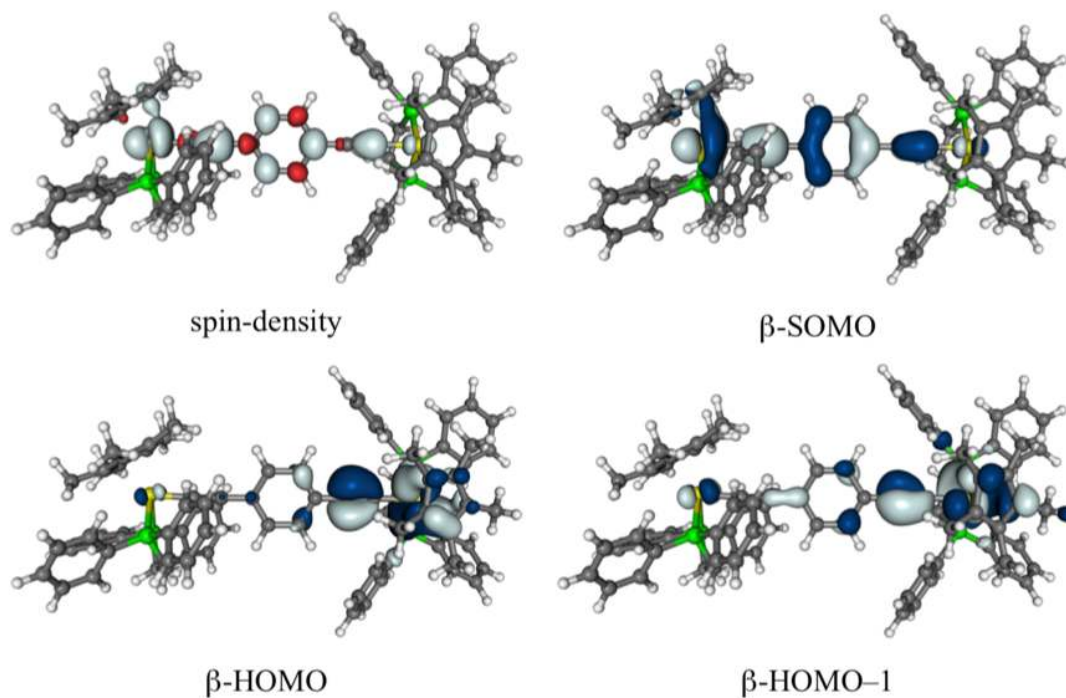
Figure 10. Isosurface plots of the spin-density (top left, $\pm$ 0.002 a.u.) and key orbitals ($\pm$ 0.03 a.u.) involved in the NIR excitations of conformer ***perp*-[1-Me]$^+$** (BLYP35/def2-SVP/COSMO(DCM)).

In order to experimentally test these proposed assignments, the solvatochromic behavior of the NIR band envelope was also examined. A sample of [**1**]PF$_6$ (prepared from **1** by treatment with AgPF$_6$) was prepared and the NIR spectrum recorded in solutions of CH$_2$Cl$_2$ and CH$_2$Cl$_2$/acetone (1:6) (Figure 11). In the more polar mixture the high energy shoulder (attributed by the computational study to the IVCT transition of the Class II component, Figure 7) shifts to higher energy and gains intensity while the main lower energy feature (attributed to the β-HOMO to β-SOMO transition which has substantial bridge π–π* character in the Class III component, Figure 5) is essentially not solvatochromic.
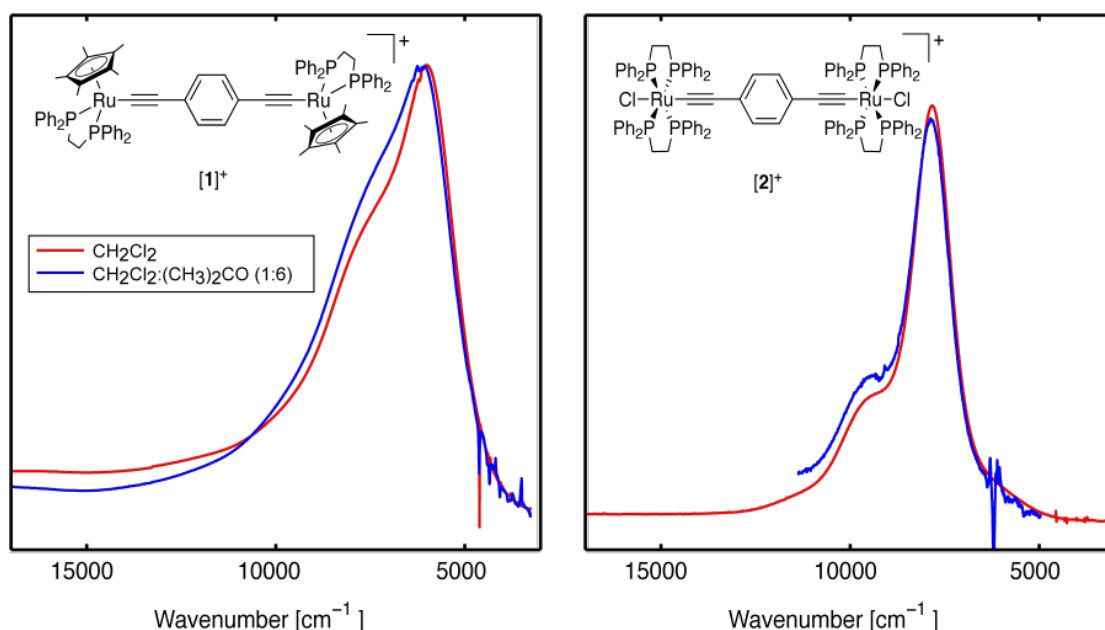
Figure 11. Overlay plots of the NIR spectra of [**1**]$^+$ and [**2**]$^+$ obtained by chemical oxidation in differing solvent mixtures.

Experimentally, the IR spectrum of [**1**]$^+$ features one very strong, one strong and two weak bands in the $\nu(C{\equiv}C)$ stretching region, as well as a medium-strong band assigned to an aryl breathing mode at lower frequency (Figure 3, cf. Table 1).[22] As noted above, these observations are inconsistent with a pure sample of a symmetrically delocalized class III complex, which should exhibit only one $\nu(C{\equiv}C)$ band, whereas the aryl breathing mode should be IR inactive for an essentially centrosymmetric system. The appearance of the IR spectrum was previously attributed to the population of structures with delocalized and localized electronic structures in solution, and suggested to be due to a distribution of conformers.[22] This proposal can now be refined through the computational work undertaken here, with the availability of three fully optimized conformational minima for [**1**]$^+$ allowing a detailed analysis of the experimental IR spectra by performing harmonic vibrational frequency analyses for all three structures (analogous results for the truncated model [**1-Me**]$^+$ are provided in Supporting Information). Harmonic vibrational frequency analyses for *trans*-[**1**]$^+$ and *cis*-[**1**]$^+$ each provide one intense $\nu(C{\equiv}C)$ band at 1978 cm^{-1} and 1987 cm^{-1}, respectively (scaled values, cf. Computational Details), which are consistent with the most intense features in the experimental spectrum (Table 1, Figure 3). Aryl breathing vibrations obtain negligible IR intensity for both of these minima. In contrast, the calculations for conformer *perp*-[**1**]$^+$ provide two $\nu(C{\equiv}C)$ frequencies of 2031 cm^{-1} and 1957 cm^{-1}, as well as a $\nu(aryl)$ mode with

23

significant intensity at 1566 cm^{-1}. The splitting of the ν(C≡C) mode and the presence of the aryl breathing mode are fully consistent with the symmetry-broken class II nature and permanent dipole moment of this conformer.[48,49] Given that **perp**-[**1**]$^+$ is higher in energy than either **trans**-[**1**]$^+$ or **cis**-[**1**]$^+$ and thus will be less populated, the lower intensities of its features at 2061 cm^{-1}, 1915 cm^{-1} and 1564 cm^{-1} in the overall experimental spectrum are easily understandable. The conformational PES is very shallow in the area around **perp**-[**1**]$^+$, but such minima may be sufficiently long-lived on the IR time scale to contribute to the spectrum. That is, the presence of rotamers with charge-localized character explains not only the shape and solvatochromic properties of the components of the NIR band envelope, but also the multiple features in the IR spectrum of [**1**]$^+$.

Table 1. Comparison of computed IR and NIR parameters for three conformational minima of [**1**]$^+$ with experimental data.[a]

conformer	infrared (IR)		near infrared (NIR)	
	ν(C≡C) [cm^{-1}] ($I_{rel.}$ [%])	ν(aryl) [cm^{-1}] ($I_{rel.}$ [%])	ν_{max}(π-π*) [cm^{-1}] (μ_{trans} [D])	ν_{max}(MLCT) [cm^{-1}] (μ_{trans} [D])
trans-[**1**]$^+$	1978 (100)	/	6566 (17.5)	/
cis-[**1**]$^+$	1987 (100)	/	6515 (17.6)	/
perp-[**1**]$^+$	2031 (100)	1566 (59)	/	9138 (10.6)
	1957 (58)			9412 (7.4)
				14248 (2.3)
exp.[22] [**1**]$^+$	2061 (w)	1564 (m)	5600[b]	6600[b]
	1997 (s)			8300[b]
	1974 (vs)			
	1915 (w)			

[a] BLYP35/def2-SVP/COSMO(DCM) level. [b]From Gaussian deconvolution of the experimental NIR absorption band envelope (accuracy disputable, see text).

Extension to [2]$^+$. Can the simultaneous presence of valence-trapped and delocalized MV conformers for a single molecule in solution explain otherwise anomalous spectroscopic data in other systems? The complex [(*trans*-Ru(dppe)$_2$Cl)$_2$(μ-C≡CC$_6$H$_4$C≡C)]$^+$,[23,29] [**2**]$^+$ offers a more symmetrical supporting

ligand environment than the half-sandwich moieties in $[\mathbf{1}]^+$. Klein et al.[23] have studied $[\mathbf{2}]^+$ by UV-vis-NIR, IR and EPR spectroscopies. The NIR spectrum collected here in DCM / 0.1 M NBu_4BF_4 is identical to that reported earlier in THF / 0.1 M NBu_4PF_6,[23] and exhibits an intense peak with an apparent peak maximum at 6550 cm^{-1}, a distinct high-energy shoulder near 8290 cm^{-1}, giving a profile similar to that of $[\mathbf{1}]^+$. In addition, a very weak low-energy shoulder near 4807 cm^{-1} also appears to be present in the NIR spectrum of $[\mathbf{2}]^+$.[23] The IR spectrum of $[\mathbf{2}]^+$ also exhibited multiple features that could not be reconciled with a simple class III description (see below) and which were thought to indicate that the system was not fully delocalized on the IR time scale.[23]

A similar 2D conformational relaxed scan as discussed above for $[\mathbf{1\text{-}Me}]^+$ was performed for the truncated system $[\mathbf{2\text{-}Me}]^+$, with dmpe replacing the dppe ligands in $[\mathbf{2}]^+$. Given the more symmetrical metal coordination environment, the end-group dihedral angle Ω was varied only from 0° to 90°, and the bridge dihedral angle Θ_{eff} from 0° to 90° (both in steps of 10°; DCM solvent model was again used, see Computational Details). The conformational PES is shown in Figure S3 in Supporting Information. Interestingly, the surface is even much shallower than that obtained above for $[\mathbf{1\text{-}Me}]^+$ and all points are within an energy of less than 8 kJ/mol. The lowest energy is obtained for $\Omega \approx 0°$, $\Theta_{eff} \approx 0°$, the highest (at 7.6 kJ/mol) for $\Omega \approx 10°$, $\Theta_{eff} \approx 90°$. A wide trough is found around $\Theta_{eff} = 0°$, but all features are much less pronounced than for $[\mathbf{1\text{-}Me}]^+$. Obviously, the dependence of electronic coupling between the redox centers on conformation is reduced due to the more symmetric coordination sphere. Given the extremely flat conformational profile, the outcome of full structure optimizations depended markedly on starting structure, obviously reflecting small numerical inaccuracies (DFT integration grids, thresholds for optimization). Large low-energy motions throughout the entire conformational phase space should be expected, and less importance attached to the specific structures at true minima on the PES compared to the deeper minima observed for $[\mathbf{1\text{-}Me}]^+$. Nevertheless, it can be noted that, for example, the lowest-energy structure obtained from a full optimization with $\Omega \approx 0°$, $\Theta_{eff} \approx 0°$ (in the following termed *deloc*-$[\mathbf{2\text{-}Me}]^+$) exhibits a fully delocalized and essentially symmetrical spin-density distribution ($Cl(dmpe)_2Ru$ / $Ru(dmpe)_2Cl$: 24 % / 22 %, Figure 12) and differences between $d(Ru-C_1)$ bond lengths in each half of the molecule of less than 0.003 Å. In

contrast, a second minimum with $\Omega \approx 45°$, $\Theta_{eff} \approx 45°$ (at 2.3 kJ/mol, in the following termed *sb*-[**2-Me**]$^+$) exhibits incipient symmetry breaking in both the spin-density (Cl(dmpe)$_2$Ru / Ru(dmpe)$_2$Cl: 34 % / 16 %; Figure 9) and in the d(Ru-C$_1$) bond lengths differing by 0.025 Å. Still more pronounced charge localization is found for other points on the PES (Figure S4).
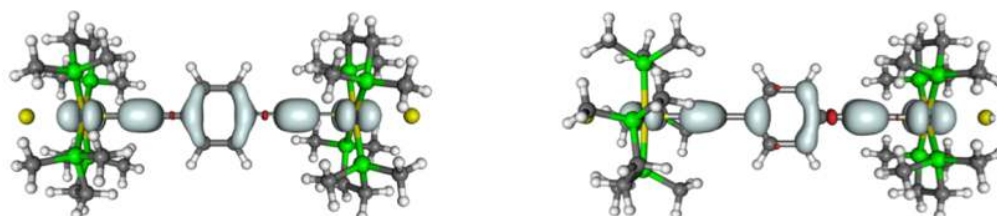

Figure 12. Spin-density isosurface plots (± 0.002 a.u.) of ***deloc*-[2-Me]**$^+$ and ***sb*-[2-Me]**$^+$ (BLYP35/def2-SVP/COSMO(DCM) level).

TDDFT results (BLYP35/def2-SVP/COSMO(DCM) level) for points across the entire 2D PES of [**2-Me**]$^+$ were obtained and an applied Boltzmann weighting used to compare the computational results with the experimental NIR band (Figure 13). The intense peak and the high- and low-energy shoulders seen experimentally in [**2**]$^+$ are reproduced by the truncated model [**2-Me**]$^+$, but the high-energy shoulder is somewhat too close to the main peak.
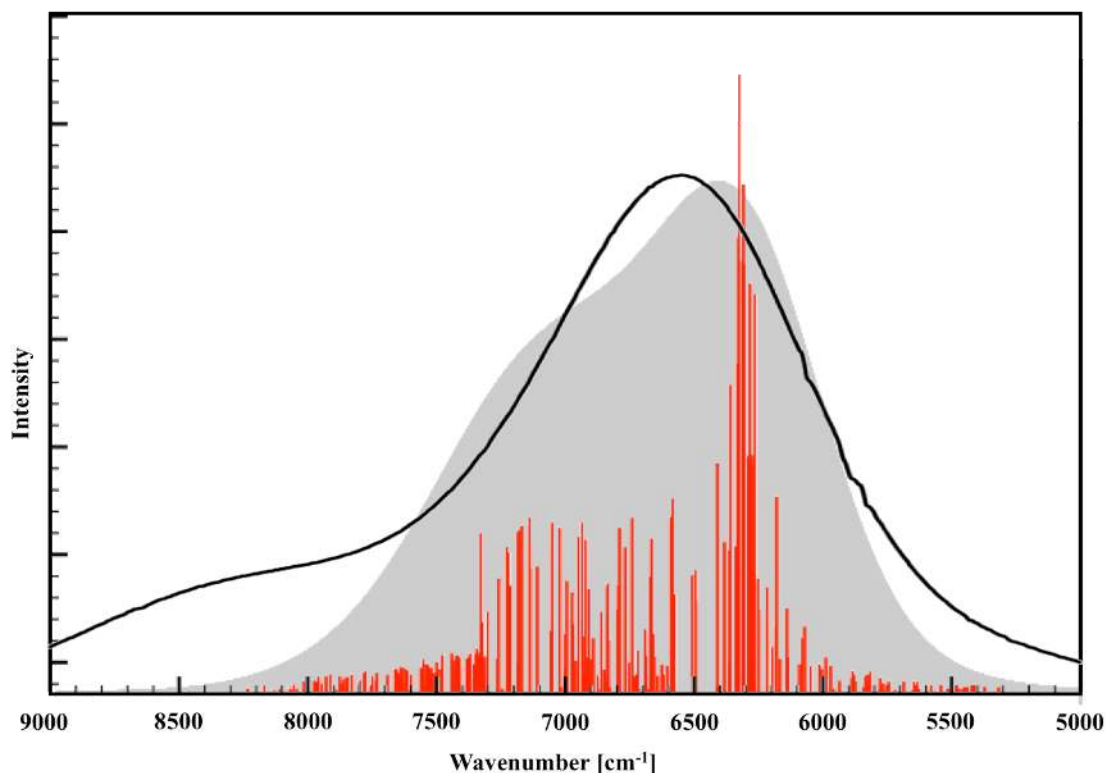
Figure 13. Computed Boltzmann-weighted TDDFT stick spectra (red) with Gaussian broadened envelope ($\sigma = 300$ cm^{-1}, FWHM = 706.4 cm^{-1}, grey) for [**2-Me**]$^+$ compared to experimental IVCT band[23] (black) of [**2**]$^+$.

The minima ***deloc*-[2-Me]**$^+$ and ***sb*-[2-Me]**$^+$ are used to illustrate how the shape of the NIR band is affected by conformational motion, but we again emphasize that structures from across the entire PES contribute to the observed spectroscopic profile. TDDFT calculations for ***deloc*-[2-Me]**$^+$ give one very intense ($\mu_{trans} = 16.7$ D) excitation at 6301 cm^{-1}, which can be assigned to the main absorption feature in the experimental spectrum. This π-π* transition occurs from the β-HOMO to the β-SOMO (Figure S5 in Supporting Information) and corresponds to the IVCT or charge resonance band associated with a delocalized (or class III) complex. A second, weaker excitation at 7392 cm^{-1} ($\mu_{trans} = 2.8$ D) is also calculated. This transition is of mixed character, as both the β-HOMO–2$\rightarrow\beta$-SOMO (64 %) and β-HOMO–1$\rightarrow\beta$-SOMO (29 %) excitation contribute significantly. The β-HOMO–2 and β-HOMO–1 are nearly degenerate (their energies differ by only 484 cm^{-1}) and are located on opposite metal centers. Given the delocalized nature of the β-SOMO, this transition may be assigned MLCT character, and it corresponds to a bridge-to-metal hole transfer. However, this transition appears to be too close in energy to those responsible for the main absorption band at 6550 cm^{-1} to fully explain the observed high-energy shoulder at 8290 cm^{-1}.

TDDFT calculations on *sb*-[**2-Me**]$^+$ reveal a main transition at 6716 cm^{-1} (μ_{trans} = 15.6 D) originating from a β-HOMO→β-SOMO excitation with π-π* character, that is blue-shifted relative to that in *deloc*-[**2-Me**]$^+$. A second excitation at 8040 cm^{-1} (μ_{trans} = 4.1 D) originates solely from the β-HOMO–1→β-SOMO transition with MLCT character (Figure S5) and appears to be better matched to the 8290 cm^{-1} absorption. Due to partial charge localization, mixing of this excitation with another MLCT transition is absent here (the near-degeneracy of β-HOMO–2 and β-HOMO–1 is lifted, their energies differ by 3647 cm^{-1}), explaining the blue shift and the enhanced intensity of this excitation compared to *deloc*-[**2-Me**]$^+$. In addition, *sb*-[**2-Me**]$^+$ exhibits a third, low-intensity TDDFT transition at 5931 cm^{-1} (μ_{trans} = 1.7 D) with more distinct β-HOMO–2→β-SOMO composition and also MLCT character (Figure S5). This transition may be connected to the experimentally observed low-energy shoulder at 4807 cm^{-1}. Thus, in *sb*-[**2-Me**]$^+$ the MLCT transitions associated with the valence trapped forms occur at both higher and lower energy than the primary IVCT (or charge resonance) band associated with the delocalized (or class III) forms. Overall, it is clear that bridge conformational motion again is responsible for the weaker features of the NIR band of [**2**]$^+$, albeit in a somewhat different manner than for [**1**]$^+$. The weakly solvatochromic nature of the NIR spectrum of [**2**]PF$_6$ when measured in CH$_2$Cl$_2$ and CH$_2$Cl$_2$/acetone (1:6) (Figure 10) also supports these assignments drawn from the models based on various conformations of [**2-Me**]$^+$.

Klein *et al*. report three experimental IR frequencies for solutions of [**2**]$^+$ at 2068 cm^{-1} (m), 1966 cm^{-1} (vs) and 1570 cm^{-1} (s) in DCM / 0.1M NBu$_4$PF$_6$.[23] Closer inspection of the data from samples in DCM / 0.1 M NBu$_4$BF$_4$ gave peaks at 2068 cm^{-1} (w), 2007 cm^{-1} (sh), 1966 cm^{-1} (vs), 1916 cm^{-1} (sh), 1807 cm^{-1} (vw), 1571 cm^{-1} (m) (Figure 3). The two minima *deloc*-[**2-Me**]$^+$ and *sb*-[**2-Me**]$^+$ allow a rationalization of the main IR bands. Only one ν(C≡C) frequency at 1985 cm^{-1} is computed for *deloc*-[**2-Me**]$^+$, and this likely contributes to the observed band at 1966 cm^{-1}. In contrast, the slight localization and symmetry breaking for *sb*-[**2-Me**]$^+$ suffices to generate two ν(C≡C) stretching frequencies at 1990 cm^{-1} (rel. intensity 31 %) and 1974 cm^{-1} (100 %), which may correlate with the experimentally observed features at 2007 cm^{-1} and 1966 cm^{-1}, and one aryl breathing mode at 1584 cm^{-1} (7 %). Due to the less pronounced localization the splitting of ν(C≡C) stretching frequencies is smaller than for [**1**]$^+$, although we cannot exclude contributions from

other areas of the PES which may help explain the other smaller features at 2068 cm^{-1} and 1916 cm^{-1}. The notion of a flatter PES and more, shallow minima calculated for [**2-Me**]$^{+}$ is consistent with the experimental spectrum of [**2**]$^{+}$, as the aryl breathing mode at 1571 cm^{-1} and the ν(C≡C) bands at 2007 and 1966 cm^{-1}, which can be attributed to a class II form of the complex, are less intense for [**2**]$^{+}$ than the analogous features in [**1**]$^{+}$ (Figure 3).

Table 2. Comparison of computed IR and NIR parameters for two conformational minima of [**2-Me**]$^{+}$ with experimental data of [**2**]$^{+}$.[a]

conformer	infrared (IR)		near infrared (NIR)	
	ν(C≡C) [cm^{-1}] ($I_{rel.}$ [%])	ν(aryl) [cm^{-1}] ($I_{rel.}$ [%])	$\nu_{max}(\pi-\pi^*)$ [cm^{-1}] (μ_{trans} [D])	ν_{max}(MLCT) [cm^{-1}] (μ_{trans} [D])
deloc-[**2-Me**]$^{+}$	1982 (100)	/	6301 (16.7)	/
	/		/	7392 (2.8)
sb-[**2-Me**]$^{+}$	1990 (31)	1584 (7)	6716 (15.6)	5931 (1.7)
	1974 (100)			8040 (4.1)
exp. [**2**]$^{+}$	2068 (w)	1571 (m)	6550[c]	8290[c]
	2007 (sh)			4807[c]
	1966 (vs)	1807 (vw)[b]		
	1916 (sh)			

[a] BLYP35/def2-SVP/COSMO(DCM) level. [b]Likely from contaminant. [c]Centers of the experimental NIR absorption band envelope.

The Creutz-Taube Ion [3]$^{5+}$. The prototypical MV complex, the Creutz-Taube ion, provides an obvious means through which to explore conformation effects in systems that ostensibly resemble [**1**]$^{+}$ and [**2**]$^{+}$. The main differences in [**3**]$^{5+}$ compared to [**1**]$^{+}$ or [**2**]$^{+}$ are the classical Werner-type coordination environment of the ruthenium centers (ammonia and pyrazine ligands coordinated to the metal center by their nitrogen atoms[6,7,24]) in the Creutz-Taube ion, the higher local symmetry at the metal centers (C$_{4v}$) and the larger positive charge. No attempt has been made here to include counter ions in the structural models but it can be assumed that some screening of charge is affected by the continuum-solvent treatment. Compound [**3**]$^{5+}$

has probably been investigated more extensively than any other MV complex, through detailed experimental measurements in the solid state[50,51] and in solution,[24,52,53] and also using quantum-chemical methods.[54-59] The UV-vis-NIR spectrum of [**3**]$^{5+}$ exhibits a single asymmetric band envelope with no notable shoulders (preventing simple Gaussian fitting). The asymmetric band shape can be explained by vibronic coupling,[1,15] which is not considered here.

For comparison with the other two systems of this study, a 2D relaxed conformer scan was conducted, varying the end-group N_{eq}-Ru-Ru-N_{eq} dihedral Ω and the N_{eq}-Ru-N_{bridge}-C_1 bridge dihedral Θ_{eff} both from 0° to 45° in steps of 5°. In contrast to [**1**]$^{+}$ and [**2**]$^{+}$, the PES of [**3**]$^{5+}$ (computed in acetonitrile, MeCN, for comparison with experimental conditions; cf. Figure S6 in Supporting Information) is dominated by a single minimum at $\Omega = 0°$, $\Theta_{eff} = 0°$. In this conformation, the plane of the bridging pyrazine ring bisects the angle between neighboring amine ligands. A single maximum is obtained at $\Omega = 0°$, $\Theta_{eff} = 45°$, indicating the eclipsing of the equatorial amine ligands by the bridge to dominate the energy profile. This maximum has a relative energy of ca. 28 kJ/mol, giving the conformational PES an energy window comparable to that of [**1**]$^{+}$ (see above). Full structure optimization of [**3**]$^{5+}$ confirms the $\Omega = 0°$, $\Theta_{eff} = 0°$ as a true minimum. Interestingly, this structure exhibits slight symmetry breaking, as indicated by two different Ru-N_{bridge} bond lengths (2.027 Å vs 2.017 Å). Nevertheless, the spin-density distribution is essentially delocalized (Figure 14). In contrast to [**1**]$^{+}$ and [**2**]$^{+}$, the BLYP35/def2-SVP/COSMO(MeCN) calculations exhibit appreciable spin contamination $<S^2> = 0.99$ (compared to 0.75 for a pure doublet state). This is manifested in the appreciable (but unphysical) negative spin-density on the bridging pyrazine (Figure 14, left; Table S4 in Supporting Information). Comparable spin contamination problems in open-shell transition-metal complexes in other calculations with hybrid density functionals have been noted previously.[60,61] In all cases examined so far, this has been connected with significant metal-ligand antibonding character of the singly occupied molecular orbital(s) (cf. Figure 14, middle).
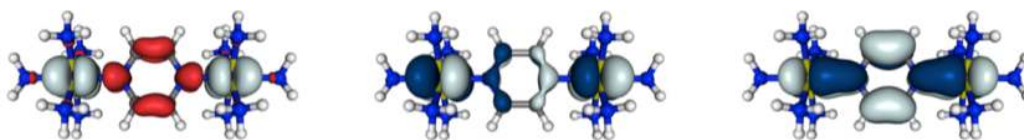
Figure 14. Isosurface plots of the spin-density (left, ± 0.002 a.u.) and β-SOMO (middle)/β-HOMO (right) (± 0.03 a.u.) of $[\mathbf{3}]^{5+}$ (BLYP35/def2-SVP/COSMO(MeCN) level).

In spite of the spin contamination, TDDFT calculations for the minimum energy structure give a single π-π^* excitation at 7046 cm^{-1} (μ_{trans} = 10.4 D), in good agreement with experimental band maximum at 6250 cm^{-1} (Gaussian 09 with its different solvent model provides 6210 cm^{-1}, in even better agreement with experiment). A complete Boltzmann-weighted sum of TDDFT stick spectra across the entire conformational 2D PES provides, in addition to the most intense peak from the minimum energy structure, blue-shifted peaks arising from the higher-energy regions of the PES. For example, the maximum at Ω = 0°, Θ_{eff} = 45° exhibits a localized spin-density, ($(NH_3)_5$Ru / pyrazine / Ru$(NH_3)_5$, 93 % / -7 % / 9 %) and a single excitation at 8198 cm^{-1}. But, due to the lower intensity (μ_{trans} = 4.4 D) and the Boltzmann weighting, this excitation barely contributes to the observed NIR spectrum. Therefore, although the calculations suggest that dynamic conformational processes in $[\mathbf{3}]^{5+}$ can shift the electronic character from localized to delocalized, in contrast to $[\mathbf{1}]^{+}$ or $[\mathbf{2}]^{+}$, the most localized forms of the Creutz-Taube ion are almost NIR silent and so there is no appreciable distortion of the experimentally observed band envelope by transitions arising from variations in the relative orientation of the $\{Ru(NH_3)_5\}^{n+}$ and the bridging ligand.

Conclusions

Delocalized class III and valence-trapped class II structures may be part of a conformational continuum for mixed-valence transition-metal complexes such as $[\mathbf{1}]^{+}$, $[\mathbf{2}]^{+}$ and $[\mathbf{3}]^{5+}$, rendering an assignment to a single Robin-Day class inappropriate. The present study suggests that conformational dynamics should be considered when a) the electronic coupling depends significantly on the conformational degrees of freedom to allow switching between delocalized and valence-trapped structures, and b) the energy landscape associated with these changes is sufficiently shallow to allow thermal sampling of delocalized and localized areas at the given temperature. Based on a suitable quantum-chemical protocol, it has been shown that these conditions hold

for the complexes $[\{Ru(dppe)Cp^*\}_2(\mu\text{-}C\equiv CC_6H_4C\equiv C)]^+$, $[\mathbf{1}]^+$ and $[\{trans\text{-}RuCl(dppe)_2\}_2(\mu\text{-}C\equiv CC_6H_4C\equiv C)]^+$, $[\mathbf{2}]^+$, to a varying extent: the conformational dependences in $[\mathbf{1}]^+$ and its truncated model $[\mathbf{1\text{-}Me}]^+$ were found to be stronger than in $[\mathbf{2}]^+$ (or $[\mathbf{2\text{-}Me}]^+$), resulting in a particularly shallow conformational profile for the latter, where the significance of minima is only marginal.

Both in $[\mathbf{1}]^+$ and $[\mathbf{2}]^+$ the conformational sampling of delocalized and valence-trapped structures is necessary and sufficient to explain a) the non-trivial shape of the IVCT band in the near-IR, and b) the simultaneous observation of vibrational frequencies in the IR consistent with class II and III behavior. In turn, the ability to simulate these spectra with the chosen quantum-chemical approach lends strong support to its correct description of the delocalized and valence-trapped portions of the conformational continuum, consistent with previous successful applications of the protocol to various organic (and partly transition-metal) mixed-valence systems. The conformation analysis for the third system studied in the present work, the classical Creutz-Taube ion $[\mathbf{3}]^{5+}$, also showed both delocalized and valence-trapped structures. However, its simulated near-IR spectrum suggests that the bands from valence-trapped conformers do not affect the overall band shape significantly, unlike the observed and simulated near-IR bands for $[\mathbf{1}]^+$ and $[\mathbf{2}]^+$.

The Robin-Day classification system will, undoubtedly, remain an important vehicle for the description of MV complexes. The present work serves to highlight that the asymmetries observed in NIR band shapes of MV complexes may not be due entirely to electronic coupling effects, but may be complicated by the presence of multiple conformers each with different electronic couplings. These effects are most significant in systems of low symmetry with relatively flat potential energy surfaces, and reinforces the essential role that the concerted application of vibrational and electronic spectroscopic methods play in determining the best overall class, or across which range of classes, a complex may belong. Together with the descriptions of MV systems to a continuum of MV classes, the availability of reliable quantum chemical methods to describe localization/delocalization in mixed-valence systems also opens the door to a much more detailed combined analysis of spectroscopic data and electronic structure in mixed-valence systems than hitherto possible. ~~It will, for example, be of interest to include further aspects omitted from the present study, such as vibronic coupling, counter-ion effects, further conformers (such as the dppe-phenyl~~

~~orientations in [**1**]^+ and [**2**]^+) and an even more elaborate treatment of the dynamics of the system at hand (including solvent dynamics).~~

Associated Content

Plots of the cut through the PES for $\Omega = 180°$ with corresponding spin densities, of the TDDFT transition dipole moment μ_{trans} of the third and fourth excitation of [**1-Me**]$^+$. Comparison of computed and experimental IR data for three conformational minima of [**1-Me**]$^+$. NIR data and spin-density contributions for three conformational minima of [**1-Me**]$^+$ and [**1**]$^+$. PES and color plot of Mulliken spin-density differences of [**2-Me**]$^+$ and [**3**]$^{5+}$. Isosurface plots of key orbitals of *sb*-[**2-Me**]$^+$. Computed Boltzmann-weighted TDDFT stick spectra and spin-density and orbital contributions of [**3**]$^{5+}$. Details of the spectroelectrochemical experiments used to obtain spectroscopic data from [**2**]$^+$. Comparison of the spectra of [**2**]$^+$ in THF / 0.1M NBu$_4$PF$_6$[23] and DCM / 0.1M NBu$_4$BF$_4$ (this work). Details of the solvatochromic experiments used to obtain the data in Figure 11. Complete reference 26.

Author information

Corresponding Authors
paul.low@uwa.edu.au
martin.kaupp@tu-berlin.de

Acknowledgment

References

(1) Heckmann, A.; Lambert, C. *Angew. Chem. Int. Ed.* **2012**, *51*, 326.
(2) Day, P.; Hush, N. S.; Clark, R. J. H. *Philos. T. Roy. Soc. A* **2008**, *366*, 5.
(3) Demadis, K. D.; Hartshorn, C. M.; Meyer, T. J. *Chem. Rev.* **2001**, *101*, 2655.
(4) Ward, M. D. *Chem. Soc. Rev.* **1995**, *24*, 121.
(5) Launay, J. P. *Chem. Soc. Rev.* **2001**, *30*, 386.
(6) Creutz, C.; Taube, H. *J. Am. Chem. Soc.* **1969**, *91*, 3988.
(7) Creutz, C.; Taube, H. *J. Am. Chem. Soc.* **1973**, *95*, 1086.
(8) Low, P. J. *Dalton Trans.* **2005**, 2821.
(9) Hush, N. S. *Electrochim. Acta* **1968**, *13*, 1005.
(10) Hush, N. S. *Coord. Chem. Rev.* **1985**, *64*, 135.
(11) Creutz, C.; Newton, M. D.; Sutin, N. *J. Photochem. Photobiol. A-Chem.* **1994**, *82*, 47.

(12)   Robin, M. B.; Day, P. *Adv. Inorg. Chem. Radiochem.* **1967**, *10*, 247.

(13)   Lear, B. J.; Chisholm, M. H. *Inorg. Chem.* **2009**, *48*, 10954.

(14)   Brunschwig, B. S.; Sutin, N. *Coord. Chem. Rev.* **1999**, *187*, 233.

(15)   Brunschwig, B. S.; Creutz, C.; Sutin, N. *Chem. Soc. Rev.* **2002**, *31*, 168.

(16)   Parthey, M.; Gluyas, J. B. G.; Schauer, P. A.; Yufit, D. S.; Howard, J. A. K.;
         Kaupp, M.; Low, P. J. **2013**, *19*, 9780

(17)   Renz, M.; Theilacker, K.; Lambert, C.; Kaupp, M. *J. Am. Chem. Soc.* **2009**,
         131, 16292.

(18)   Kaupp, M.; Renz, M.; Parthey, M.; Stolte, M.; Würthner, F.; Lambert, C.
         Phys. Chem. Chem. Phys. **2011**, *13*, 16973.

(19)   Renz, M.; Kaupp, M. *J. Phys. Chem. A* **2012**, *116*, 10629.

(20)   Renz, M.; Kess, M.; Diedenhofen, M.; Klamt, A.; Kaupp, M. *J. Chem. Theory
         Comput.* **2012**, *8*, 4189.

(21)   Völker, S. F.; Renz, M.; Kaupp, M.; Lambert, C. *Chem. Eur. J.* **2011**, *17*,
         14147.

(22)   Fox, M. A.; Le Guennic, B.; Roberts, R. L.; Brue, D. A.; Yufit, D. S.; Howard,
         J. A. K.; Manca, G.; Halet, J.-F.; Hartl, F.; Low, P. J. *J. Am. Chem. Soc.* **2011**,
         133, 18433.

(23)   Klein, A.; Lavastre, O.; Fiedler, J. *Organometallics* **2006**, *25*, 635.

(24)   Creutz, C.; Chou, M. H. *Inorg. Chem.* **1987**, *26*, 2995.

(25)   TURBOMOLE V6.4 **2012**, a development of University of Karlsruhe and
         Forschungszentrum Karlsruhe GmbH, 1989-2007, TURBOMOLE GmbH,
         since 2007.

(26)   Frisch, M. J.; et al. ; *Gaussian 09*; Revision A.02 ed.; Gaussian, Inc.:
         Wallingford, CT, **2009**.

(27)   Boese, A. D.; Martin, J. M. L. *J. Chem. Phys.* **2004**, *121*, 3405.

(28)   Yanai, T.; Tew, D. P.; Handy, N. C. *Chem. Phys. Lett.* **2004**, *393*, 51.

(29)   Lavastre, O.; Plass, J.; Bachmann, P.; Guesmi, S.; Moinet, C.; Dixneuf, P. H.
         Organometallics **1997**, *16*, 184.

(30)   Krejcik, M.; Danek, M.; Hartl, F. *J. Electroanal. Chem.* **1991**, *317*, 179.

(31)   Klamt, A.; Schüürmann, G. *J. Chem. Soc., Perkin Trans. 2* **1993**, *5*, 799.

(32)   Barone, V.; Cossi, M. *J. Phys. Chem. A* **1998**, *102*, 1995.

(33)   Cossi, M.; Rega, N.; Scalmani, G.; Barone, V. *J. Comput. Chem.* **2003**, *24*,
         669.

(34)   Klamt, A. *J. Phys. Chem.* **1996**, *100*, 3349.

(35)   Scalmani, G.; Frisch, M. J.; Mennucci, B.; Tomasi, J.; Cammi, R.; Barone, V.
         J. Chem. Phys. **2006**, *124*.

(36)   Schäfer, A.; Horn, H.; Ahlrichs, R. *J. Chem. Phys.* **1992**, *97*, 2571.

(37)   Weigend, F.; Ahlrichs, R. *Phys. Chem. Chem. Phys.* **2005**, *7*, 3297.

(38)   Andrae, D.; Häussermann, U.; Dolg, M.; Stoll, H.; Preuss, H. *Theor. Chim.
         Acta* **1990**, *77*, 123.

(39)   Scott, A. P.; Radom, L. *J. Phys. Chem.* **1996**, *100*, 16502.

(40)   Roder, J. C.; Meyer, F.; Hyla-Kryspin, I.; Winter, R. F.; Kaifer, E. *Chem. Eur.
         J.* **2003**, *9*, 2636.

(41)   U. Varetto*, MOLEKEL 5.4*, Swiss National Supercomputing Centre: Manno,
         Switzerland.

(42)   MatLab *R2012b (8.0.0783)*, **2012**, The MathWorks Inc., Natick,
         Massachusetts.

(43)   Pelmenschikov, V.; Guo, Y.; Wang, H.; Cramer, S. P.; Case, D. A. *Faraday
         Discuss.* **2011**, *148*, 409.

(44)   Schauer, P. A.; Low, P. J. *Eur. J. Inorg. Chem.* **2012**, *2012*, 390.

(45)   Ward, M. D.; McCleverty, J. A. *J. Chem. Soc., Dalton Trans.* **2002**, 275.

(46)   Armitt, D. J.; Bruce, M. I.; Gaudio, M.; Zaitseva, N. N.; Skelton, B. W.; White, A. H.; Le Guennic, B.; Halet, J. F.; Fox, M. A.; Roberts, R. L.; Hartl, F.; Low, P. J. *Dalton Trans.* **2008**, 6763.

(47)   Eichkorn, K.; Weigend, F.; Treutler, O.; Ahlrichs, R. *Theor. Chem. Acc.* **1997**, *97*, 119.

(48)   Fox, M. A.; Roberts, R. L.; Baines, T. E.; Le Guennic, B.; Halet, J.-F.; Hartl, F.; Yufit, D. S.; Albesa-Jové, D.; Howard, J. A. K.; Low, P. J. *J. Am. Chem. Soc.* **2008**, *130*, 3566.

(49)   Fox, M. A.; Farmer, J. D.; Roberts, R. L.; Humphrey, M. G.; Low, P. J. *Organometallics* **2009**, *28*, 5266.

(50)   Furholz, U.; Joss, S.; Burgi, H. B.; Ludi, A. *Inorg. Chem.* **1985**, *24*, 943.

(51)   Hush, N. S.; Edgar, A.; Beattie, J. K. *Chem. Phys. Lett.* **1980**, *69*, 128.

(52)   Oh, D. H.; Sano, M.; Boxer, S. G. *J. Am. Chem. Soc.* **1991**, *113*, 6880.

(53)   Petrov, V.; Hupp, J. T.; Mottley, C.; Mann, L. C. *J. Am. Chem. Soc.* **1994**, *116*, 2171.

(54)   Bencini, A.; Ciofini, I.; Daul, C. A.; Ferretti, A. *J. Am. Chem. Soc.* **1999**, *121*, 11418.

(55)   Reimers, J. R.; Cai, Z. L.; Hush, N. S. *Chem. Phys.* **2005**, *319*, 39.

(56)   Bolvin, H. *Inorg. Chem.* **2007**, *46*, 417.

(57)   Reimers, J. R.; Wallace, B. B.; Hush, N. S. *Philos. T. Roy. Soc. A* **2008**, *366*, 15.

(58)   Hardesty, J.; Goh, S. K.; Marynick, D. S. *Theochem-J. Mol. Struct.* **2002**, *588*, 223.

(59)   Todorova, T.; Delley, B. *Inorg. Chem.* **2008**, *47*, 11269.

(60)   Munzarova, M.; Kaupp, M. *J. Phys. Chem. A* **1999**, *103*, 9966.

(61)   Remenyi, C.; Kaupp, M. *J. Am. Chem. Soc.* **2005**, *127*, 11399.